ISA Transactions 151 (2024) 377–390

Contents lists available at ScienceDirect

ISA Transactions

journal homepage: www.elsevier.com/locate/isatrans

Practice article

Remote path-following control for a holonomic Mecanum-wheeled robot in a resource-efficient networked control system

Rafael Carbonell [a], Ángel Cuenca [a,*], Julián Salt [a], Ernesto Aranda-Escolástico [b], Vicente Casanova [a]

[a] Instituto Universitario de Automática e Informática Industrial, Universitat Politècnica de València, 46022 Valencia, Spain
[b] Departamento de Ingeniería de Software y Sistemas Informáticos, Universidad Nacional de Educación a Distancia, 28040 Madrid, Spain

ARTICLE INFO

Keywords:
Networked control
Periodic event-triggered communication
Kalman filter
Stochastic stability
Mecanum-wheeled robot

ABSTRACT

This paper introduces a novel resource-efficient control structure for remote path-following control of autonomous vehicles based on a comprehensive combination of Kalman filtering, non-uniform dual-rate sampling, periodic event-triggered communication, and prediction-based and packet-based control techniques. An essential component of the control solution is a non-uniform dual-rate extended Kalman filter (NUDREKF), which includes an h-step ahead prediction stage. The prediction error of the NUDREKF is ensured to be exponentially mean-square bounded. The algorithmic implementation of the filter is straightforward and triggered by periodic event conditions. The main goal of the approach is to achieve efficient usage of resources in a wireless networked control system (WNCS), while maintaining satisfactory path-following behavior for the vehicle (a holonomic Mecanum-wheeled robot). The proposal is additionally capable of coping with typical drawbacks of WNCS such as time-varying delays, and packet dropouts and disorder. A Simscape Multibody simulation application reveals reductions of up to 93% in resource usage compared to a nominal time-triggered control solution. The simulation results are experimentally validated in the holonomic Mecanum-wheeled robotic platform.

1. Introduction

Holonomic mobile robots are characterized by freely moving in any direction [1]. They are usually equipped with omnidirectional wheels, e.g., Mecanum wheels [2], which make wheeled robots highly maneuverable and suitable for narrow spaces or crowded environments such as industrial plants, warehouses, hospitals, military tasks, and space exploration. In the present work, a holonomic mobile platform, which is built on four Mecanum wheels, is considered. The robot is additionally supplied with a beacon-based indoor positioning system, which introduces two technological issues: (i) it is battery-powered, and hence, every time the robot position is taken and delivered, the battery life is reduced; (ii) the data processing needed to determine the robot position is time-consuming, which forces to set slower sensing rates. Designing a controller for the mobile robot at this slow rate may be problematic for reaching some desired specifications. However, slow-rate battery usage may be beneficial to enlarge battery life. Integrating periodic event-triggered communication (PETC) and long sensing periods may further increase system resource efficiency.

PETC is based on the combination of event-triggered sampling (see, e.g., [3]) and the traditional time-triggered sampling. In the PETC paradigm, the conditions to transmit the system measurements are evaluated periodically. As a discrete-time mechanism, PETC results in a straightforward implementation, where a minimum inter-event time is guaranteed, avoiding Zeno behavior [4]. As a consequence of its benefits, PETC has becoming a trending research topic in the last years, extending its application to a wide variety of fields (for instance: unmanned ground or aerial vehicles [5,6], multi-agent systems [7], human–robot cooperation [8], robotic manipulators [9], tank processes [10], cyber–physical systems [11], DC microgrids [12], hard-disk drives [13], etc.). Most of these applications present a recurrent framework: networked control systems (NCS).

NCS gives attention to control scenarios where a common communication link is shared by different connected devices, enabling suitable

* Corresponding author.
E-mail addresses: racarla1@inf.upv.es (R. Carbonell), acuenca@isa.upv.es (Á. Cuenca), julian@isa.upv.es (J. Salt), earandae@issi.uned.es (E. Aranda-Escolástico), vcasanov@isa.upv.es (V. Casanova).

https://doi.org/10.1016/j.isatra.2024.05.041
Received 7 November 2023; Received in revised form 24 May 2024; Accepted 24 May 2024
Available online 27 May 2024

control structures for remote path-following control of autonomous vehicles. NCS has been applied in various areas, such as industrial control systems [14], automobiles [15], teleoperation [16], etc. In our work, the control solution is remotely located from sensors, actuators and plant with the aim of delegating the computation of the control algorithm to a powerful remote station. The remote control structure is composed of an advanced extended Kalman filter [17], an enhanced adaptation of the Pure Pursuit path-tracking algorithm [18], and a dynamic controller based on the inverse kinematic model of the robot. As a resource-efficient approach, the processor governing the local devices is chosen to be a low-power device with limited processing and storage capabilities. The most computationally complex part of the control algorithm is given by the extended Kalman filter. Its total computational cost is $O(n^3)$ [19]. As a consequence of the networked control structure proposed, this significant amount of computational resources is saved by the local processor, avoiding possible performance degradation. NCS introduces not only advantages such as cost and weight reduction, and modularity, but also drawbacks like the possible existence of packet dropouts [20], time-varying delays [21], packet disorder [22], and bandwidth constraints [23]. In this work, a remote path-following control for the Mecanum-wheeled robotic platform is proposed in a wireless NCS (WNCS), where (i) the network bandwidth usage is reduced by taking advantage of the PETC mechanism, (ii) time-varying delays and packet dropouts are addressed by the advanced Kalman filter, and (iii) the packet disorder phenomenon can be evaded by making use of the large sensing period forced by the beacon system. Resource-efficient WNCS approaches [24,25] mainly aim at decreasing computation burden and network load, and increasing battery life of the wireless devices connected to the network. These approaches can be found in a wide spectrum of practical applications such as cooperative transport [26], agriculture irrigation [27], wind turbines [28], rehabilitation therapy [29], etc.

As previously pointed out, if the control system were designed at the slow rate forced by the measurement system, control performance may be degraded, or even may become unstable. In this work, this issue is solved by using a dual-rate extended Kalman filter [30], which becomes an essential component of the control solution. The filter is able to generate fast-rate robot state estimates from slow-rate robot output data. Providing these estimations to the Pure Pursuit algorithm and to the dynamic controller, suitable fast-rate control actions can be computed in order to reach acceptable path following.

Since sensor-to-controller packet dropouts can occur, or the event-triggered conditions may not hold, a scarce, slow-rate measurement signal may be received by the filter. For this reason, a non-uniform version of the dual-rate extended Kalman filter (NUDREKF) is needed. The filter is formulated and straightforwardly implemented to work under the PETC mechanism. As a result, the filter is able to work irrespective of possible delayed measurements, and the amount of computations required is reduced. The prediction error of the NUDREKF is ensured to be exponentially mean-square bounded.

In order to deal not only with the scarce data from sensors but also with controller-to-actuator packet dropouts and delayed control signals, the filter integrates an h-step ahead prediction stage. The prediction structure is capable to calculate a group of h estimated control actions, which is transmitted to the plant side (actuators) following packet-based control techniques [31].

Packet-based control allows us to lower the transmission rate by simultaneously transferring a group of data. After a successful delivery, the preceding set of control actions will be replaced by the new, updated one at the actuators, and then, irrespective of the network-induced delay, the consequent control actions can be applied while no new packet is received.

To the best of the authors' knowledge, very few works can be found in literature coping with state estimation for non-uniform dual-rate sampled-data non-linear systems using Kalman filtering techniques. The approach is used to treat infrequent and delayed data in [32,33], and missing data in [34]. In [35], both time-varying delays and packet dropouts are faced in an in-vehicle WNCS environment, where the filter is formulated and implemented to work in a time-driven fashion. As a consequence, the solution is executed at every control period, requiring a higher number of computations than in the event-triggered version proposed in the present work.

The control solution has been simulated using Simscape Multibody (a Matlab-Simulink tool) to include complex, non-linear dynamics, and real-word physical constraints that are present in the real vehicle (e.g., dead-zone, actuator saturation, encoder resolution, wheel slip, floor conditions, and so on). To the best of authors' knowledge, Simscape Multibody has been used in few works to simulate Mecanum-wheeled mobile platforms (e.g., in [34,36,37]). No work integrating a network model has been found. The simulation results have been experimentally validated in the holonomic robotic platform.

Summarizing, the work gathers these main contributions:

- A resource-efficient path-following control structure based on a comprehensive combination of Kalman filtering, non-uniform dual-rate sampling, periodic event-triggered communication, and prediction-based and packet-based control techniques.
- Formulation and straightforward implementation of a NUDREKF in a periodic event-driven working mode. Mean-square stability conditions are given for the filter.
- A robust simulation application for a WNCS scenario, which reveals an excellent trade-off between energy efficiency and path-following behavior for the proposed control solution compared to time-triggered approaches. Real experiments on a holonomic Mecanum-wheeled robotic platform validate the simulation results.

The paper is organized as follows. Section 2 is dedicated to notation, robot modeling aspects, and problem scenario. Section 3 formulates the control solution and analyzes its stability. Section 4 is focused on simulation results. Section 5 is devoted to the experimental validation. Finally, in Section 6, some conclusions and future works sum up the present work.

2. Notation, robot modeling, and problem scenario

Fig. 1 illustrates the resource-efficient control approach proposed in this work, where two main parts are distinguished:

- Remote side, where the control solution is implemented (details in Section 3).
- Local side, which includes the robot environment, a smart actuator to properly inject the control signal, and a sensor that incorporates a PETC mechanism.

Both sides are connected by means of a wireless network, which may induce some drawbacks such as packet dropout and disorder, and time-varying delays. These drawbacks are formally described in Section 2.3. The kinematic modeling of the robotic platform is introduced in Section 2.1. Details about the PETC mechanism are presented in Section 2.2, and the working mode of the control solution is detailed in Section 2.4.

As a dual-rate solution, two different rates, or periods, are considered: the (fast) control period is T, and the (slow) measurement period is NT, being $N \in \mathbb{N}^+$ the multiplicity. A T-period variable or signal is denoted as $(.)_k^T$, and a NT-period variable or signal as $(.)_k^{NT}$. $k \in \mathbb{N}$ is

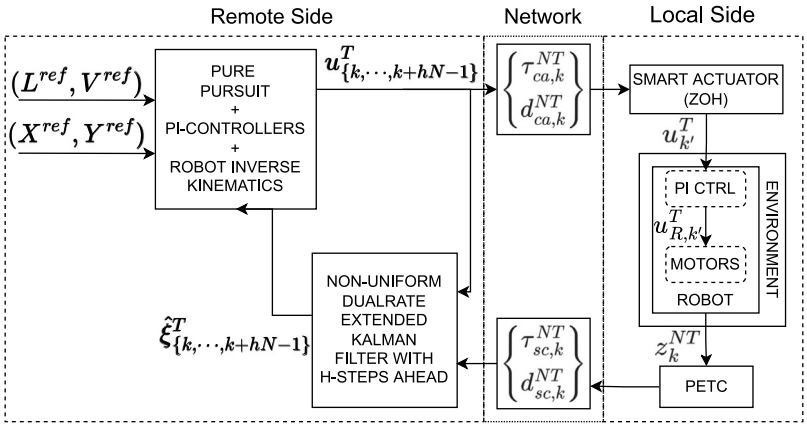

Fig. 1. Resource-efficient networked control system.

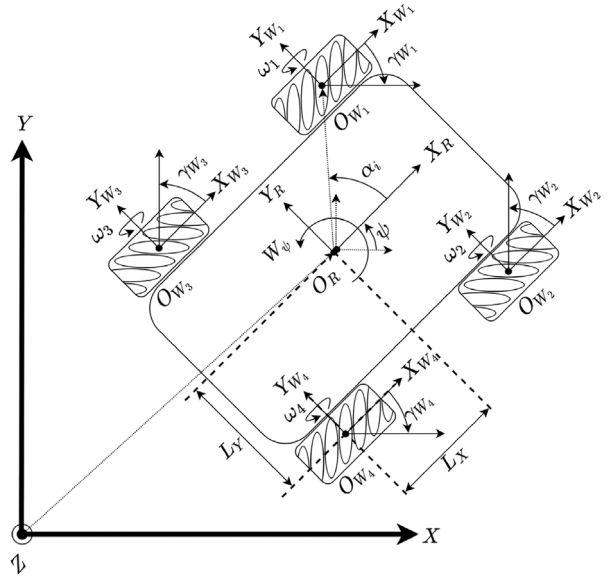

Fig. 2. Kinematic model.

used to represent iterations at T or NT, respectively. In the sequel, $[\cdot]^\top$ means transpose function, and $\mathbb{E}[\cdot]$ is the expectation.

2.1. Kinematic modeling of the robotic platform

From Fig. 2, the kinematic model of the robot can be deduced in discrete time at period T (see, e.g., [38], for more details):

$$
\begin{aligned}
(V_x)_k^T &= \left((\omega_1)_k^T + (\omega_2)_k^T + (\omega_3)_k^T + (\omega_4)_k^T\right)\frac{R}{4},\\
(V_y)_k^T &= \left(-(\omega_1)_k^T + (\omega_2)_k^T + (\omega_3)_k^T - (\omega_4)_k^T\right)\frac{R}{4},\\
(W_\psi)_k^T &= \left(-(\omega_1)_k^T + (\omega_2)_k^T - (\omega_3)_k^T + (\omega_4)_k^T\right)\frac{R}{4(L_x+L_y)},\\
X_k^T &= X_{k-1}^T + (V_x)_k^T T\cos(\psi_{k-1}^T + (W_\psi)_k^T T)\\
&\quad - (V_y)_k^T T\sin(\psi_{k-1}^T + (W_\psi)_k^T T),\\
Y_k^T &= Y_{k-1}^T + (V_x)_k^T T\sin(\psi_{k-1}^T + (W_\psi)_k^T T)\\
&\quad + (V_y)_k^T T\cos(\psi_{k-1}^T + (W_\psi)_k^T T),\\
\psi_k^T &= \psi_{k-1}^T + (W_\psi)_k^T T,
\end{aligned}
\tag{1}
$$

where $(\omega_1,\omega_2,\omega_3,\omega_4)_k^T$ are the rotational velocities of each wheel, $(V_x,V_y)_k^T$ are the longitudinal and lateral velocities, $(W_\psi)_k^T$ is the orientation, $(X,Y,\psi)_k^T$ is the posture, L_x and L_y are the longitudinal and lateral distances, respectively, and R is the radius of every wheel.

As low-speed motion of the vehicle is used in this work (less than 5 m/s), a reasonable assumption about null slip angles at front and rear wheels can be assumed in the kinematic model [39].

From $(X,Y)_k^T$ in (1), the distances $(d_1,d_2,d_3,d_4)_k^T$ from each of the four fixed beacons to the mobile one can be obtained. Let us define $\{(X_1,Y_1),(X_2,Y_2),(X_3,Y_3),(X_4,Y_4)\}$ as the position of every fixed beacon on the base reference frame, Z_{fb} as the height with respect to the ground plane (the same value for each fixed beacon), and Z_{mb} as the height for the mobile beacon. Finally, the conversion, which is based on the Pythagorean theorem, [40], yields to:

$$
(d_i)_k^T = \sqrt{\left(X_i - X_k^T\right)^2 + \left(Y_i - Y_k^T\right)^2 + \left(Z_{fb} - Z_{mb}\right)^2}, \quad i = 1..4 \tag{2}
$$

2.2. Periodic event-triggered condition

The event-triggered condition is periodically evaluated at the instants kNT. Using the scheduling variable $\beta_k^{NT} \in \{0,1\}$ at the sensor, the output data $z_k^{NT} = (\omega_1,\omega_2,\omega_3,\omega_4,\psi,d_1,d_2,d_3,d_4)_k^{NT}$ will be sent through the network when $\beta_k^{NT} = 1$. Otherwise, when $\beta_k^{NT} = 0$, the data are not sent. Let us use $\bar{z}_k^{NT}$ to keep the latest sensor data

$$
\bar{z}_k^{NT} = \beta_k^{NT} z_k^{NT} + (1-\beta_k^{NT})\bar{z}_{k-1}^{NT}, \tag{3}
$$

for $k \in \mathbb{N}_{\geq 1}$, and where $\bar{z}_0^{NT} = z_0^{NT}$. From a mixed event-triggered strategy [41] on z_k^{NT}, the periodic condition at the sensor devices can be defined as follows

$$
\sum_{i=1}^{s} \|\bar{z}_{k-1}^{NT}(i) - z_k^{NT}(i)\|^2 > \sum_{i=1}^{s} \sigma(i)\|z_k^{NT}(i)\|^2 + \delta(i), \tag{4}
$$

for $k \in \mathbb{N}_{\geq 1}$, where $s = size(z_k^{NT})$, $\bar{z}_0^{NT} = z_0^{NT}$, $\delta(i)$ are positive constants, and $\sigma(i) \in \{0,1\}$ (as recommended in [42]). Optimal values for the event-triggered parameters $\delta(i)$ and $\sigma(i)$ can be reached by following Montecarlo-like procedures [35], leading to an excellent trade-off between resource savings and control performance.

2.3. Packet dropout and disorder, and time-varying delays

In our scenario, packet dropouts may occur as a random phenomenon [43], and can be modeled as a Bernoulli distribution. The possible sensor-to-controller and controller-to-actuator packet dropouts are respectively denoted as $d_{sc,k}^{NT}$ and $d_{ca,k}^{NT}$. The probability of dropout p_{sc} and p_{ca} that contemplates both Bernoulli processes can be expressed as:

$$
\begin{aligned}
p_{sc} &= \Pr[d_{sc,k}^{NT} = 0] \in [0,1),\\
p_{ca} &= \Pr[d_{ca,k}^{NT} = 0] \in [0,1).
\end{aligned}
\tag{5}
$$

The network-induced delay for a packet that includes the outputs sensed at instant kNT and is actually delivered (i.e., the trigger condition (4) holds, and $p_{sc} = p_{ca} = 0$) can be defined as

$$\tau_k^{NT} = \tau_{s,k}^{NT} + \tau_{sc,k}^{NT} + \tau_{c,k}^{NT} + \tau_{ca,k}^{NT}, \tag{6}$$

being $\tau_{s,k}^{NT}$ the processing time at the sensor devices to determine all the robot outputs, $\tau_{sc,k}^{NT}$ the sensor-to-controller delay, $\tau_{c,k}^{NT}$ a controller's computation time delay, and $\tau_{ca,k}^{NT}$ the controller-to-actuator delay. For simplicity, let us lump together $\tau_{s,k}^{NT}$ with $\tau_{sc,k}^{NT}$, and $\tau_{c,k}^{NT}$ with $\tau_{ca,k}^{NT}$.

In this work, packet disorder will be evaded by forcing the maximum delay $\tau_{max} = \max(\tau_k^{NT})$ to fulfill $\tau_{max} < NT$. The maximum delay τ_{max} can be deduced from the delay distribution. In our scenario, a generalized exponential distribution may be considered [44]. Then, the probability density function is given by

$$P[\tau_k^{NT}] = \begin{cases} \frac{1}{\phi} e^{\frac{-(\tau_k^{NT} - \eta)}{\phi}} & \text{if } \tau_k^{NT} \geq \eta, \\ 0 & \text{if } \tau_k^{NT} < \eta, \end{cases} \tag{7}$$

where the variable ϕ may be deduced from $\mathbb{E}[\tau_k^{NT}]$ and η. The value η may be obtained from the median of the delay.

2.4. Control structure

Next, the working mode of the different blocks in Fig. 1 is detailed:

- When an event is triggered according to (4), and the packet from sensors is not lost (i.e., $d_{sc,k}^{NT} = 1$), the NUDREKF receives the vehicle measurements $z_k^{NT} = (\omega_1, \omega_2, \omega_3, \omega_4, \psi, d_1, d_2, d_3, d_4)_k^{NT}$ after a delay $\tau_{sc,k}^{NT}$. Then, it computes the prediction and correction of the process state $\hat{\xi}_k^T = (\hat{V}_x, \hat{V}_y, \hat{W}_\psi, \hat{X}, \hat{Y}, \hat{\psi})_k^T$ (details in Section 3.3.1).
- From the kinematic reference (X^{ref}, Y^{ref}) and the estimated position $(\hat{X}, \hat{Y})_k^T$, the Pure Pursuit algorithm computes the reference linear velocities, $(V_x^{ref}, V_y^{ref})_k^T$, considering a desired speed V^{ref}, and a look ahead distance L^{ref}. Note that, for this purpose, as the mobile platform will follow 2D paths, the reference positions (X^{ref}, Y^{ref}) are only needed, setting to 0 the reference orientation $(\psi^{ref} = 0)$. More details in Section 3.1.
- Some PI controllers receive the reference velocities $(V_x^{ref}, V_y^{ref})_k^T$ and the reference orientation $(W_\psi^{ref})_k^T$ (obtained from the orientation estimate $\hat{\psi}_k^T$) to calculate the velocity and orientation control signals $(V_x^u, V_y^u, W_\psi^u)_k^T$, which are transformed into the dynamic references $u_k^T = (\omega_1^{ref}, \omega_2^{ref}, \omega_3^{ref}, \omega_4^{ref})_k^T$ by following (9) in Section 3.2.
- The complete set of state estimates $\hat{\xi}_{\{k,\dots,k+hN-1\}}^T$ and dynamic references $u_{\{k,\dots,k+hN-1\}}^T$ are computed by the h-step ahead prediction stage added to the NUDREKF. The set of dynamic references will be packaged and transmitted to the plant side. More details in Section 3.3.1.
- If the packet is received by the smart actuator after a delay $\tau_{ca,k}^{NT}$, the actuator will replace the previous packet with the new one, and choose the right control action from the new set, that is, $u_{k'}^T$, $k' \in \{k, \dots, k+hN-1\}$. Then, PI controllers located inside the robot environment will compute the control signal $u_{R,k'}^T$. The next control actions of the current packet will be consecutively injected at period T, while no new packet is received. Then, the robot is always receiving control actions at period T irrespective of the delay and packet dropouts, which enables to reach satisfactory path-following control properties.

Fig. 3 illustrates a time axis example, where $\hat{\xi}_{j|i}^T$ and $u_{R,j|i}^T$ respectively denote the state estimate and the control action generated for the T-instant j at the NT-period i. As it can be seen, at the beginning of the period kNT, the control actions previously received and computed in the period $(k-1)NT$ are being injected. When a new packet arrives to the controller, the new groups of state estimates and dynamic

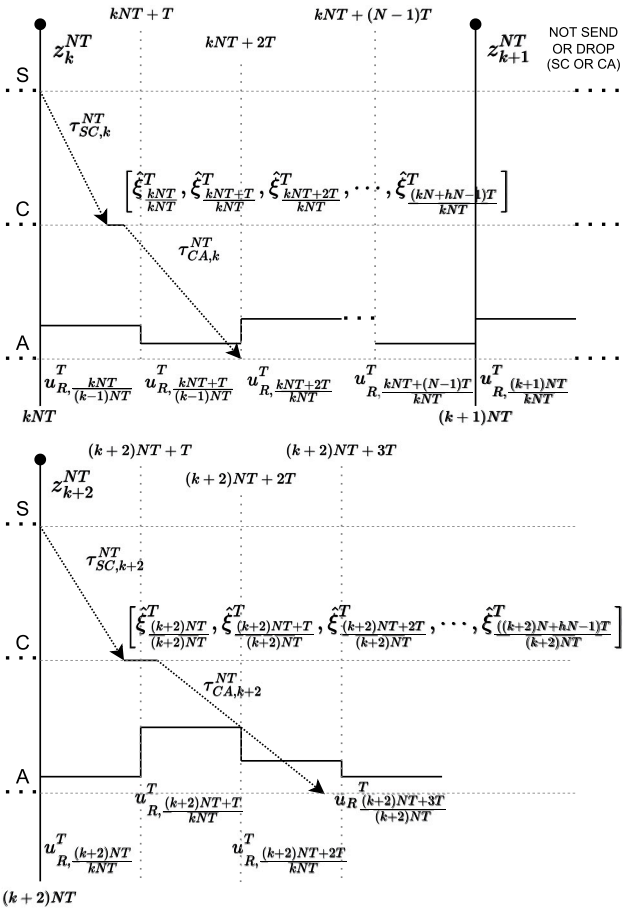

Fig. 3. Time axis example (S: Sensor, C: Controller, A: Actuator).

references are computed for the period kNT. The actuator will receive the new packet after a round-trip time delay $\tau_k^{NT} = 2T$, and hence, the action to be applied will be $u_{R,kNT+2T|kNT}$. While no new packet arrives, the next control actions of the packet computed in the period kNT will be injected every T instants of time. In the period $(k+2)NT$, a new packet is successfully delivered, repeating the process. Now, the delay is $\tau_{k+2}^{NT} = 3T$, and hence, the action $u_{R,(k+2)NT+3T|(k+2)NT}$ will be injected.

3. Control solution

This section is devoted to introduce the remote control structure proposed in this work, which is composed of an enhanced adaptation of the Pure Pursuit path-tracking algorithm (Section 3.1), a dynamic controller based on the inverse kinematics of the robot (Section 3.2), and a non-uniform version of a dual-rate extended Kalman filter including an h-step ahead prediction stage (Section 3.3).

3.1. Enhanced adaptation of the pure pursuit path-tracking algorithm

The improved version used in this work for the Pure Pursuit path-tracking algorithm is based on decomposing the reference linear velocity V^{ref} into Cartesian components (V_x^{ref}, V_y^{ref}), which are parameterized by a variable gain K_V that depends on the distance D to the target point. As a result, the algorithm is able to improve its adaptability to the change in turning and curvature sections of paths.

In more detail, from D and the look ahead distance L^{ref}, the gain $K_V \in [0,1]$ can be obtained as $K_V = \frac{D}{L^{ref}}$. Then, considering the Cartesian components d_x and d_y of the distance D, the reference linear velocities are calculated:

$$\begin{aligned} V_x^{ref} &= V^{ref} \cdot K_V \cdot cos\left(atan2\left(\frac{d_y}{d_x}\right)\right), \\ V_y^{ref} &= V^{ref} \cdot K_V \cdot sin\left(atan2\left(\frac{d_y}{d_x}\right)\right), \end{aligned} \tag{8}$$

being $atan2$ the fourth-quadrant inverse tangent. More details about the implementation of the algorithm can be found in [34].

3.2. Dynamic controller based on the inverse kinematics of the robot

After applying the Pure Pursuit path tracking algorithm and some PI controllers, the velocity and orientation control actions $(V_x^u, V_y^u, W_\psi^u)_k^T$ are obtained. Then, the inverse kinematic model of the robot is used to transform the velocity and orientation control actions into the reference rotational velocities $u_k^T = (\omega_1^{ref}, \omega_2^{ref}, \omega_3^{ref}, \omega_4^{ref})_k^T$:

$$\begin{aligned} (\omega_1^{ref})_k^T &= \frac{1}{R}((V_x^u)_k^T - (V_y^u)_k^T - (L_x + L_y)(W_\psi^u)_k^T), \\ (\omega_2^{ref})_k^T &= \frac{1}{R}((V_x^u)_k^T + (V_y^u)_k^T + (L_x + L_y)(W_\psi^u)_k^T), \\ (\omega_3^{ref})_k^T &= \frac{1}{R}((V_x^u)_k^T + (V_y^u)_k^T - (L_x + L_y)(W_\psi^u)_k^T), \\ (\omega_4^{ref})_k^T &= \frac{1}{R}((V_x^u)_k^T - (V_y^u)_k^T + (L_x + L_y)(W_\psi^u)_k^T). \end{aligned} \tag{9}$$

where R, L_x, and L_y were defined below (1).

3.3. Non-uniform dual-rate extended Kalman filter with h-step ahead prediction stage

3.3.1. Formulation

From the robot model in (1), the NUDREKF is able to estimate the non-available robot measurements. The non-linear model can be rewritten as

$$\begin{cases} \xi_k^T = f\left(\xi_{k-1}^T, (n_1)_{k-1}^T, u_{k-1}^T\right), \\ z_k^T = h\left(\xi_k^T, (n_2)_k^T\right), \end{cases} \tag{10}$$

being $\xi_k^T = \left[(V_x, V_y, W_\psi, X, Y, \psi)_k^T\right]^\top$ the robot state; $u_{k-1}^T = [(\omega_1^{ref}, \omega_2^{ref}, \omega_3^{ref}, \omega_4^{ref})_{k-1}^T]^\top$ the control action; $z_k^T = \left[(\omega_1, \omega_2, \omega_3, \omega_4, \psi, d_1, d_2, d_3, d_4)_k^T\right]^\top$ the output; $(n_1)_{k-1}^T$ a possible process noise with covariance Q_k^T; and $(n_2)_k^T$ a possible measurement noise with covariance R_k^T.

At the sampling instants kNT when no sensor-to-controller packet dropout occur (i.e., $d_{sc,k}^{NT} = 1$), and the periodic event-triggered condition (4) holds, the prediction and correction steps of the NUDREKF are formulated in this way:

- Prediction for $\hat{\xi}_{k|k-1}^T$ and $P_{k|k-1}^T$ (being $k \in \mathbb{N}_{\geq 1}$):

$$\begin{aligned} \hat{\xi}_{k|k-1}^T &= f\left(\hat{\xi}_{k-1|k-1}^T, (n_1)_{k-1}^T, u_{k-1}^T\right), \\ P_{k|k-1}^T &= A_k^T P_{k-1|k-1}^T [A_k^T]^\top + L_k^T Q_{k-1}^T [L_k^T]^\top, \end{aligned} \tag{11}$$

where $\hat{\xi}_{0|0}^T = \mathbb{E}[\xi_0^T]$, and $P_{0|0}^T = \mathbb{E}\left[\left(\xi_0^T - \hat{\xi}_{0|0}^T\right)\left[\left(\xi_0^T - \hat{\xi}_{0|0}^T\right)\right]^\top\right]$. By means of the Jacobian matrices A_k^T and L_k^T, the process model is linearized

$$\begin{aligned} A_k^T &= \left.\frac{\partial f}{\partial \xi}\right|_{\hat{\xi}_{k-1|k-1}^T, (n_1)_{k-1}^T, u_{k-1}^T}, \\ L_k^T &= \left.\frac{\partial f}{\partial n_1}\right|_{\hat{\xi}_{k-1|k-1}^T, (n_1)_{k-1}^T, u_{k-1}^T}. \end{aligned} \tag{12}$$

- Correction for $\hat{\xi}_{k|k}^T$ and $P_{k|k}^T$:

$$\begin{aligned} \hat{\xi}_{k|k}^T &= \hat{\xi}_{k|k-1}^T + K_k^T(z_k^T - \hat{z}_k^T), \\ P_{k|k}^T &= K_k^T R_k^T [K_k^T]^\top + (I - K_k^T H_k^T) P_{k|k-1}^T [(I - K_k^T H_k^T)]^\top. \end{aligned} \tag{13}$$

where the estimated output $\hat{z}_k^T$ is given by

$$\hat{z}_k^T = h\left(\hat{\xi}_{k|k-1}^T, (n_2)_k^T\right). \tag{14}$$

and the gain of the Kalman filter K_k^T is computed as

$$K_k^T = P_{k|k-1}^T [H_k^T]^\top \left(H_k^T P_{k|k-1}^T [H_k^T]^\top + M_k^T R_k^T [M_k^T]^\top\right)^{-1}, \tag{15}$$

being H_k^T and M_k^T Jacobian matrices used to linearize the output model

$$\begin{aligned} H_k^T &= \left.\frac{\partial h}{\partial \xi}\right|_{\hat{\xi}_{k|k-1}^T, (n_2)_k^T}, \\ M_k^T &= \left.\frac{\partial h}{\partial n_2}\right|_{\hat{\xi}_{k|k-1}^T, (n_2)_k^T}. \end{aligned} \tag{16}$$

Additionally, the h-step ahead prediction stage integrated in the NUDREKF is executed with the aim of providing the fast-rate robot state estimates, which are used at the sampling instants kT until a new packet is received from sensors. The parameter h represents an upper-bound of the possible consecutive packet dropouts. As a dual-rate system, each of the h steps will compute N estimations. The prediction stage works as follows:

(1) The position $(\hat{X}, \hat{Y})_k^T$ corrected in (13) and the kinematic reference (X^{ref}, Y^{ref}) are used by the Pure Pursuit algorithm to compute the reference linear velocities, $(V_x^{ref}, V_y^{ref})_k^T$ in (8). From the corrected orientation $\hat{\psi}_k^T$, the reference orientation $(W_\psi^{ref})_k^T$ is obtained.

(2) From the references $(V_x^{ref}, V_y^{ref}, W_\psi^{ref})_k^T$ and the corrected linear velocities and orientation $(\hat{V}_x, \hat{V}_y, \hat{W}_\psi)_k^T$, the velocity and orientation control actions $(V_x^u, V_y^u, W_\psi^u)_k^T$ are computed via PI control, and then, the dynamic references u_k^T via the inverse kinematics in (9).

(3) The non-linear robot model in (10) is iterated, and the next estimates are calculated

$$\begin{cases} \hat{\xi}_{k+1}^T = f\left(\hat{\xi}_k^T, (n_1)_k^T, u_k^T\right) \\ \hat{z}_{k+1}^T = h\left(\hat{\xi}_{k+1}^T, (n_2)_{k+1}^T\right) \end{cases}. \tag{17}$$

The covariance is additionally propagated such as in (11).

(4) After N-1 iterations, the first subset of estimations is obtained, $\{\hat{\xi}_{k+1}^T, \ldots, \hat{\xi}_{k+N-1}^T\}$.

(5) Repeating Steps 1–4 h-1 times, the complete set of estimates is computed, $\{\hat{\xi}_{k+1}^T, \ldots, \hat{\xi}_{k+hN-1}^T\}$.

3.3.2. Stochastic stability

Next, stochastic stability of the NUDREKF is analyzed. Note that, if the estimation error of the NUDREKF can be bounded, then the control system, based on PI controllers, can achieve the desired performance. First, let us consider the following statistical properties:

- $\mathbb{E}\left[\xi_0^T\right] = \bar{\xi}_{0|0}^T$, $\mathbb{E}\left[\left(\xi_0^T - \bar{\xi}_{0|0}^T\right)\left(\xi_0^T - \bar{\xi}_{0|0}^T\right)^\top\right] = \hat{P}_{0|0}^T$,
- $\mathbb{E}\left[(n_1)_k^T\right] = 0$, $\mathbb{E}\left[(n_2)_k^T\right] = 0$,
- $\mathbb{E}\left[(n_1)_k^T [(n_1)_k^T]^\top\right] = Q_k^T$, $\mathbb{E}\left[(n_2)_k^T [(n_2)_k^T]^\top\right] = R_k^T$.

To deal with the dual-rate behavior and with the packet dropout at the same time, a binary variable λ_k is designed. When $\lambda_k = 0$, either there is no measurement in that instant, i.e. $(kT \mod NT) \neq 0$, or the sensor measurement is lost. On the contrary, when $\lambda_k = 1$, the measurement is transmitted normally. Note that, λ_k is not an actual random variable, since the instants of time defined by the slow period

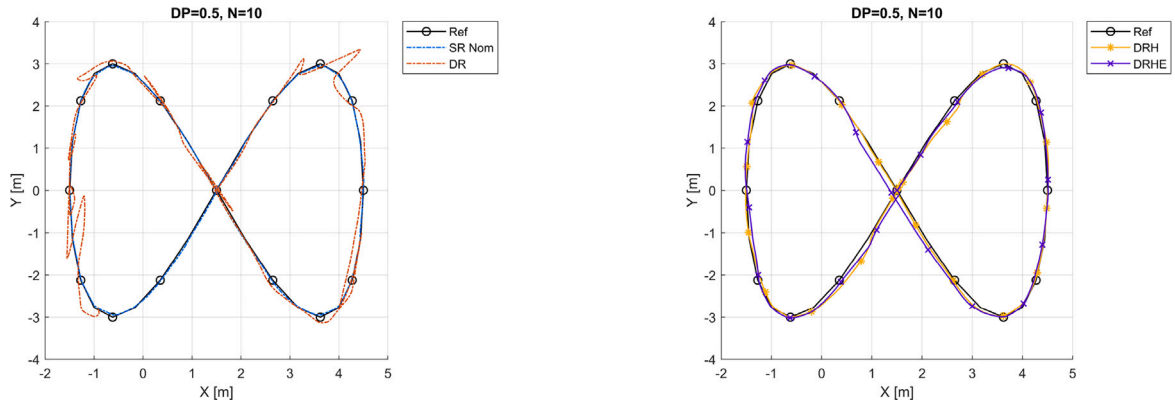

Fig. 4. Path tracking comparison for Lissajous curve in simulation ($DP = 0.5, N = 10$).

are known. However, it will be considered as a random variable to simplify the stability analysis. As a result, a constraint in the mean square of λ_k is induced, since, as a maximum, there is only one transmission in a slow period NT, i.e. $\lambda := \mathbb{E}[\lambda_k] \leq 1/N$.

Theorem 1. *For given scalars $\sigma = \max\{\sigma_i\} \geq 0$ for $i = 1, \ldots, s$, $\delta = \sum_{i=1}^{s} \delta(i) \geq 0$, $a_1 > 0$, $a_2 > 0$, $a_3 > 0$, the prediction error of the NUDREKF is exponentially bounded in mean square with bound $\mathbb{E}\left\{\left(\bar{\xi}^T_{k+1|k}\right)^2\right\} \leq \frac{\bar{p}}{\underline{p}}\mathbb{E}\left\{\left(\bar{\xi}^T_{1|0}\right)^2\right\}(1-\eta)^k + \nu\bar{p}\sum_{i=1}^{k-1}(1-\eta)^i$ if real constants $\bar{a}$, $\bar{h}$, $\underline{h}$, $\bar{k}$, $\bar{l}$, $\underline{l}$ $\bar{m}$, $\bar{p}$, $\underline{p}$, $\bar{q}$, $\underline{q}$, $\bar{r}$ such that*

$$\begin{aligned} &A_k^T \leq \bar{a}I,\ \underline{h}I \leq H_k^T \leq \bar{h}I,\ K_k^T \leq \bar{k}I, \\ &\underline{l}I \leq L_k^T \leq \bar{l}I,\ M_k^T \leq \bar{m}I, \\ &\underline{p}I \leq \bar{P}^T_{k+1|k+1} \leq \hat{P}^T_{k+1|k} \leq \bar{p}I, \\ &\underline{q}I \leq Q_k^T \leq \bar{q}I,\ R_k^T \leq \bar{r}I \end{aligned} \tag{18}$$

are satisfied $\forall k$, H_k^T is nonsingular $\forall k$, the initial prediction error is bounded, and the following inequalities are satisfied

$$\frac{1-\bar{a}^2+(1-\gamma)\bar{a}^2(1+a_1)\left(1+\bar{k}\bar{h}\right)^2+(1+a_1^{-1}+a_2^{-1})\bar{k}^2\sigma\bar{h}^2}{\gamma\bar{a}^2} < \lambda \leq 1/N, \tag{19}$$

$$0 < \frac{\underline{l}^2\underline{q}}{\bar{a}^2\bar{p}+\underline{l}^2\underline{q}} + a_3\frac{\underline{l}^2\underline{q}}{\bar{a}^2\bar{p}+\underline{l}^2\underline{q}} - a_3 - a_3^{-1}\bar{k}\sigma \leq 1, \tag{20}$$

where γ is the average sensor communication rate, $\eta = \mu + a_3\mu - a_3 - a_3^{-1}\bar{k}\sigma$, $\nu = a_3^{-1}\bar{k}^2\delta + \frac{\bar{a}^2\bar{k}^2\bar{r}+\bar{l}^2\bar{q}}{\bar{p}}$ and $\mu = \frac{\underline{l}^2\underline{q}}{\bar{a}^2\bar{p}+\underline{l}^2\underline{q}}$.

See proof in Appendix A.

4. Simulation

In this work, the Simscape Multibody application developed in [34] has been enhanced to integrate network features. This realistic simulation application includes all the specific parameters (surface friction, robot dynamics, sensor noise, actuator limitations, and so on) under which the experimentation is conducted. For more details, a shortened version of the application is available at https://github.com/CO3-UPV/Simscape_Robot_Mecanum. The application has been used with the aim of comparing the proposed control solution to other control approaches.

4.1. Cases simulated

The control proposal presented in this work is compared to three different control approaches, ranging from single-rate (SR) to dual-rate (DR) cases. Every case simulated uses the same time-varying delay distribution (with $\eta = 0.01$ and $\phi = 0.02$ in (7)) but different sampling periods ($N = [1, 2, \ldots, 12]$), and dropout probabilities ($DP = p_{sc} = p_{ca} = [0, 0.1, \ldots, 0.7]$). Next, the cases considered in the comparison are presented, being the fourth one (DRHE) the control solution proposed in this work:

- Single-rate (SR): In this case, sensing and actuation is carried out at the same period NT, being $T = 0.1$ s. Let us define the nominal single-rate case when $N = 1$ and no dropout occurs ($DP = 0$).
- Dual-rate (DR): In this case, the proposal presented in [34] is considered. The remote side receives the measurements every NT instants of time. Then, it computes N control actions, which are sent in a packet. The actuator receives and applies the actions at period T. If a packet dropout occurs, the last control action of the last packet received by the actuator is held. This case will be considered as the reference dual-rate case to be compared with the next dual-rate cases.
- Dual-rate with h-step ahead prediction stage (DRH): In this case, if packet dropouts occur, control action estimates can be applied ($h > N$ is assumed). Depending on the dropout probability and the periods considered, the number of control action estimates, hN, will take values in the range {10, 50}.
- Dual-rate with h-step ahead prediction stage and periodic event-triggered condition (DRHE): It is the same case as in DRH, but also applying control action estimates when the event condition is not triggered. Now, $hN \in \{100, 156\}$. For the lowest sampling period, i.e., when $N = 12$, then $hN = 156$, which implies to face up to $h = 13$ consecutive packet dropouts at period $NT = 1.2$ s. This corresponds to a lack of system data (dropouts, or long delays) for up to 15.6 s. The event-triggered parameters are defined as $\delta(i) = 0.1,\ i = 1..s$ in (4), and $\sigma(i) = 0.1,\ i = 1..4$; $\sigma(i) = 0.05,\ i = 5..s$ in (4).

Let us use three different reference trajectories to be tracked: a Lissajous curve (Fig. 4), a double lane change maneuver (Fig. 5), and a path including a 180° turn (Fig. 6). In all of them, $V^{ref} = 0.2$ m/s. The figures depict a comparison among the cases previously presented. The dual-rate options consider a multiplicity $N = 10$, and a dropout probability $DP = 0.5$. As shown for every trajectory, DRH and DRHE clearly outperforms DR, reaching a similar behavior to the nominal case for SR. This is mainly due to the fact that DRH and DRHE are able to cope with network problems such as time-varying delays and packet dropouts by computing future fast-rate state estimates. Additionally, by integrating the event-triggered communication mechanism, DRHE is able to reduce resource usage, as it will be analyzed in next sections.

4.2. Cost indexes

The next cost indexes will be used to assess the results in Section 4.3:

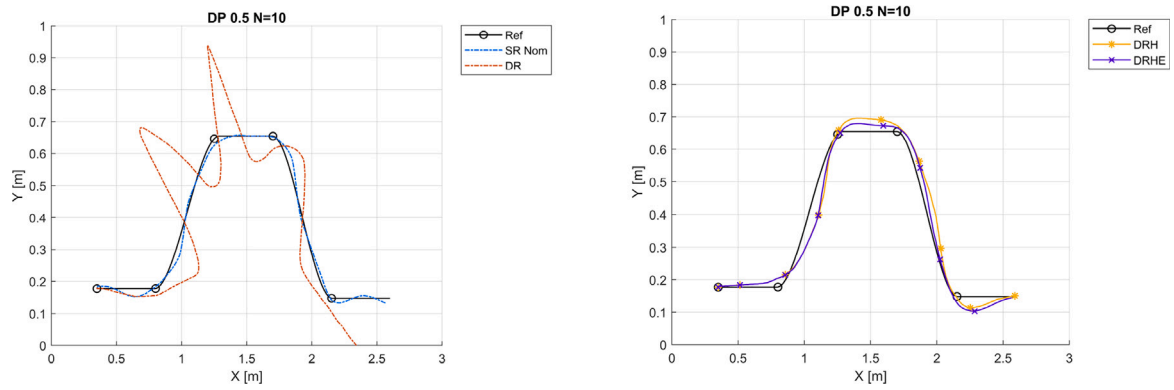

Fig. 5. Path tracking comparison for a double lane change maneuver in simulation ($DP = 0.5, N = 10$).

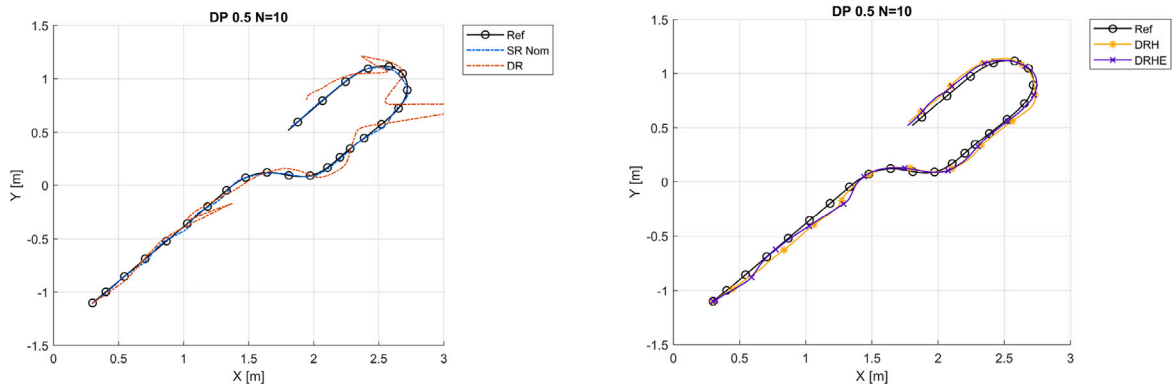

Fig. 6. Path tracking comparison for a 180° turn in simulation ($DP = 0.5, N = 10$).

- Root-mean-square error, J_1 (m):

$$J_1 = \frac{1}{l}\sum_{k=1}^{l} \min_{1\le k'\le l} \sqrt{\left(X_k^T - (X^{ref})_{k'}^T\right)^2 + \left(Y_k^T - (Y^{ref})_{k'}^T\right)^2}. \tag{21}$$

- Maximum root-square error, J_2 (m):

$$J_2 = \max_{1\le k\le l}\left\{ \min_{1\le k'\le l} \sqrt{\left(X_k^T - (X^{ref})_{k'}^T\right)^2 + \left(Y_k^T - (Y^{ref})_{k'}^T\right)^2} \right\}. \tag{22}$$

- Time elapsed, J_3 (s):

$$J_3 = lT. \tag{23}$$

- Resource usage reduction, J_4:

$$J_4 = \frac{Tr(*)}{Tr(nom)}, \tag{24}$$

which is the relation between the amount of packets transmitted by the case selected, $Tr(*)$, and the packets transmitted by the nominal single-rate time-triggered control, $Tr(nom)$.

4.3. Simulation results

As the trends observed are the same for every trajectory previously simulated, for the sake of brevity, let us only present and analyze the results obtained for the Lissajous curve. Figs. 7–10 depict the cost indexes got for this trajectory. For comparison purposes, J_1, J_2 and J_3 are normalized with respect to the nominal SR case (J_4 is already normalized by definition). A representative subset of the results are quantified in Tables 1–4. These are the main conclusions:

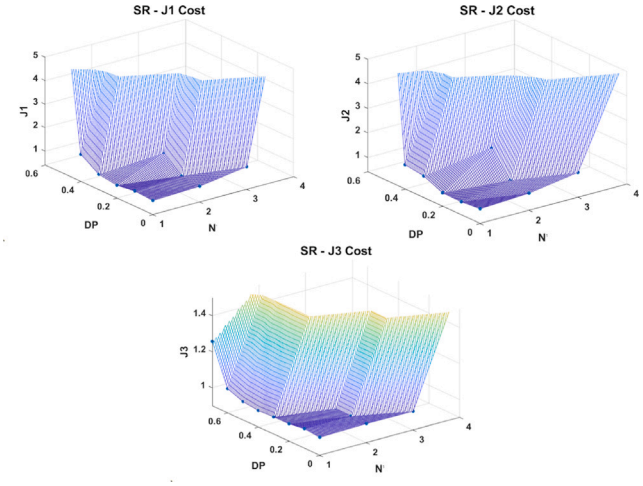

Fig. 7. Simulation results for single-rate (SR).

- According to Fig. 7, if the period NT and the packet dropout probability DP are increased with respect to the nominal single-rate (SR) case (where $N = 1$ and $DP = 0$), the cost indexes J_1, J_2 and J_3 for SR are significantly incremented, which means a clear control performance worsening. This fact is numerically quantified in the column named SR in Tables 1–3, where the unstable responses are represented by the ∞ symbol.
- In Fig. 8, a considerable improvement for every dual-rate (DR) cost index with respect to each homologous SR case is observed. This aspect is confirmed by the column named DR in Tables 1–3,

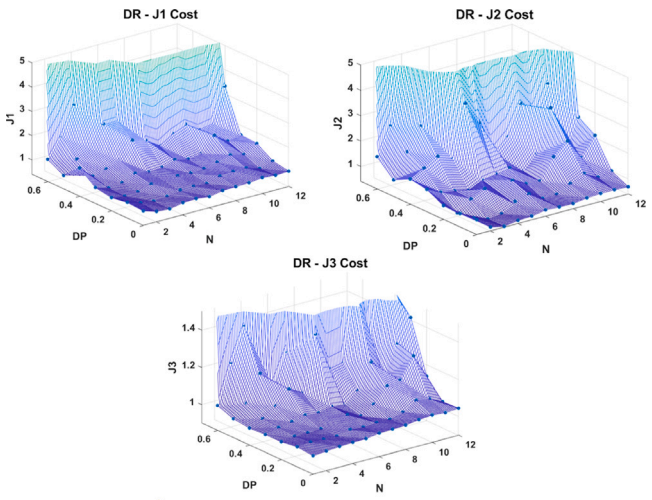

Fig. 8. Simulation results for dual-rate (DR).

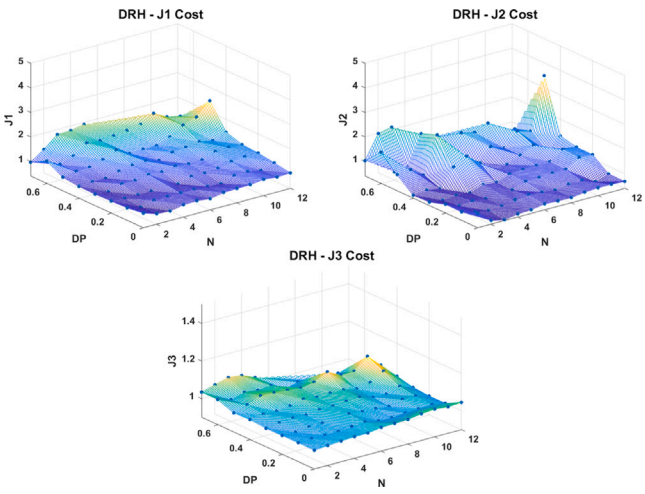

Fig. 9. Simulation results for dual-rate with h-step stage (DRH).

where lower values are presented for DR in comparison with SR. For the stable cases of SR, that is, when $N = 2$ and $DP < 0.4$, the improvement reached by DR in J_1 and J_2 is quite evident (up to 53% and 77%, respectively). For the other cases, except for $N = \{6, 12\}$ and $DP = 0.6$, DR is able to achieve stable responses versus the SR unstable behaviors. The stable responses for DR can be obtained for larger sensing periods than in the SR case, that is, N could even arrive at 12 for DR, while only at 2 for SR. As expected (and also observed in SR), for a particular N in DR, the greater DP is, the worse (higher) values for the cost indexes J_1, J_2 and J_3 will be.

- Fig. 9 shows that the cost indexes for the dual-rate case with the h-step ahead prediction stage (DRH) are noticeably decremented with respect to the DR case, except when $DP = 0$, since both approaches coincide under this condition. The improvement can be better observed as N and DP are increased. Tables 1–3 verify this achievement. For instance, considering one of the extreme cases, that is, when $N = 12$ and $DP = 0.4$, improvements around 56% in J_1, 59% in J_2, and 31% in J_3 can be reached. On average, for DRH, J_1 is reduced 29%, J_2 50%, and J_3 12% with respect to DR. It is worthy to note that the case where $N = 6$ and $DP = 0.6$ results in stable behavior for DRH versus the unstable response for DR.
- Finally, Fig. 10 depicts the excellent trade-off between control performance and resource usage reduction, which can be attained by our proposal, that is, the dual-rate case with prediction stage and event-triggered communication (DRHE). These are the main conclusions:
  - J_1, J_2 and J_3 for DRHE have slightly worsened with respect to DRH. According to Tables 1–3, on average, J_1 increases around 19%, J_2 21%, and J_3 3%. Then, DRHE achieves an average improvement of around 10% in J_1, 29% in J_2, and 9% in J_3 with respect to DR. Compared to the nominal SR case, the average worsening is also light: 28% in J_1, 2% in J_2, and 6% in J_3. As a consequence of all the percentages, an acceptable performance deterioration for DRHE is deduced.
  - As detailed in Table 4, J_4 is ranging from 0.067 (for $N = 12$ and $DP = 0$) to 0.132 (for $N = 2$ and $DP = 0.6$), which means a significant reduction in resource usage (between 87% and 93%) with respect to the nominal SR approach. Table 4 additionally shows the expected reduction in resource usage (for the stable cases) as N increases. This reduction is intensified by using DRHE. Comparing DRHE with DRH, the lower N is, the higher percentage of reduction will be reached (for $N = 2$, the reduction arrives approximately at 76%, while for $N = 12$ only at 18%). A higher N implies sending fewer packets, and hence, gives a limited room to further reductions.

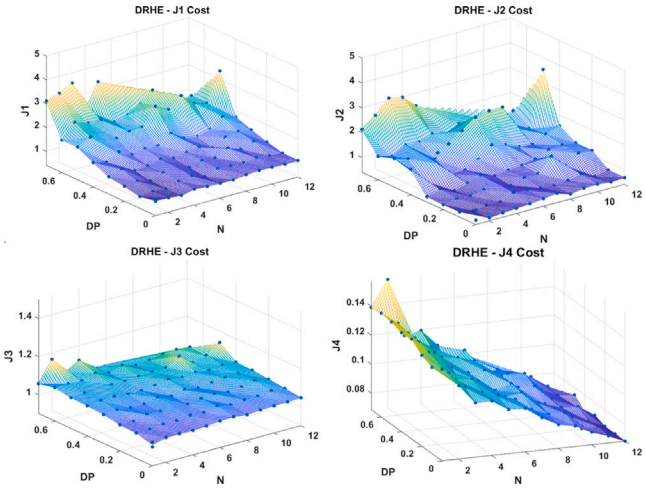

Fig. 10. Simulation results for dual-rate with h-step stage and events (DRHE).

5. Experimental validation

In this work, the test-bed robotic platform used in [34] is improved to enable remote control (see in Fig. 11). Then, an Ebyte E220 wireless communication module has been added via serial port to be used both in the robot and in the remote station. The code has been developed via Simulink with Simulink Coder for Arduino Due. In this section, the

Table 1
Results for J_1 in simulation.

J_1		SR	DR	DRH	DRHE
DP	N				
0	1	1.00	–	–	–
0.2	1	1.15	–	–	–
0.4	1	1.57	–	–	–
0.6	1	∞	–	–	–
0	2	1.07	0.83	0.83	1.01
0.2	2	1.80	0.86	0.85	1.10
0.4	2	∞	1.08	0.93	1.15
0.6	2	∞	2.15	1.03	1.37
0	6	∞	0.85	0.85	1.03
0.2	6	∞	1.12	0.86	1.09
0.4	6	∞	1.98	1.19	1.40
0.6	6	∞	∞	1.61	1.89
0	12	∞	1.02	1.02	1.10
0.2	12	∞	1.56	1.23	1.28
0.4	12	∞	3.32	1.48	1.73
0.6	12	∞	∞	∞	∞

Table 2
Results for J_2 in simulation.

J_2		SR	DR	DRH	DRHE
DP	N				
0	1	1.00	–	–	–
0.2	1	1.20	–	–	–
0.4	1	1.40	–	–	–
0.6	1	∞	–	–	–
0	2	1.10	0.56	0.56	0.58
0.2	2	2.28	0.58	0.57	0.70
0.4	2	∞	1.69	0.58	0.81
0.6	2	∞	2.80	0.73	1.21
0	6	∞	0.65	0.65	0.72
0.2	6	∞	1.22	0.68	0.84
0.4	6	∞	2.90	1.11	1.29
0.6	6	∞	∞	1.15	1.53
0	12	∞	0.68	0.68	0.70
0.2	12	∞	2.11	1.17	1.27
0.4	12	∞	3.20	1.33	1.55
0.6	12	∞	∞	∞	∞

Table 3
Results for J_3 in simulation.

J_3		SR	DR	DRH	DRHE
DP	N				
0	1	1.00	–	–	–
0.2	1	1.01	–	–	–
0.4	1	1.02	–	–	–
0.6	1	∞	–	–	–
0	2	1.02	1.01	1.01	1.03
0.2	2	1.03	1.02	1.01	1.04
0.4	2	∞	1.03	1.02	1.07
0.6	2	∞	1.25	1.03	1.08
0	6	∞	1.03	1.03	1.04
0.2	6	∞	1.05	1.03	1.05
0.4	6	∞	1.40	1.04	1.07
0.6	6	∞	∞	1.04	1.10
0	12	∞	1.04	1.04	1.05
0.2	12	∞	1.14	1.05	1.07
0.4	12	∞	1.51	1.05	1.08
0.6	12	∞	∞	∞	∞

experiments tested in the platform are shown to validate the simulation results.

5.1. Cases validated

Due to hardware limitations in the communication devices, the lowest period that can be used to send packets through the network results in $NT = 0.2s$. A representative subset of experiments is analyzed to validate the trends observed in the simulation. The cases studied consider the dropout probabilities $DP = [0, 0.1, 0.2, 0.3.0.4]$, and the multiplicities $N = [2, 4, 6]$. As a consequence of practical issues, higher DP and N result in unfeasible experiments. It is also worth noting that, due to the workspace available for experimentation, the size of the reference to be tracked has been reduced with respect to the simulation.

Figs. 12–14 depict a comparison among the different cases in the test-bed platform for every trajectory used in Section 4.1. The parameters considered for the dual-rate cases are $N = 4$ and $DP = 0.4$. These tests validate the trends observed in simulation, that is:

- DRH and DRHE reach a similar behavior to the fastest possible SR option (at 0.2s).
- DRH and DRHE clearly outperform DR, whose behavior is on the verge of instability for every trajectory in this case.

As it will be detailed in next section, DRHE is additionally able to reduce resource usage compared to DRH.

Table 4
Results for J_4 in simulation.

J_4		SR	DR	DRH	DRHE
DP	N				
0	1	1.000	–	–	–
0.2	1	1.000	–	–	–
0.4	1	1.000	–	–	–
0.6	1	∞	–	–	–
0	2	0.500	0.500	0.500	0.119
0.2	2	0.500	0.500	0.500	0.124
0.4	2	∞	0.500	0.500	0.129
0.6	2	∞	0.500	0.500	0.132
0	6	∞	0.167	0.167	0.099
0.2	6	∞	0.167	0.167	0.102
0.4	6	∞	0.167	0.167	0.105
0.6	6	∞	∞	0.167	0.108
0	12	∞	0.083	0.083	0.067
0.2	12	∞	0.083	0.083	0.068
0.4	12	∞	0.083	0.083	0.069
0.6	12	∞	∞	∞	∞

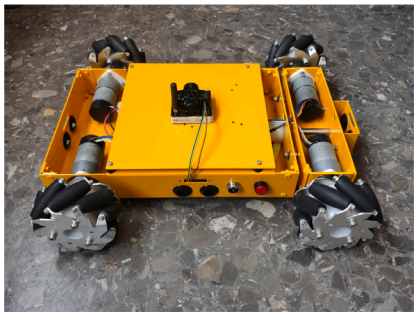

Fig. 11. Holonomic Mecanum-wheeled robot.

5.2. Experimental results

For the sake of brevity, let us focus on the DRH and DRHE cases for the Lissajous curve. Figs. 15 and 16 show the cost indexes obtained in the experimental validation, which verify the behaviors observed in simulation. A representative subset of these results are quantified in Tables 5 and 6. These are the main conclusions:

- J_1, J_2 and J_3 for DRHE have slightly worsened with respect to DRH. On average, J_1 increases around 16%, J_2 10%, and J_3 3%. J_1 and J_3 present quite similar percentages to those obtained in simulation (19% and 3%, respectively), while J_2 is a bit better

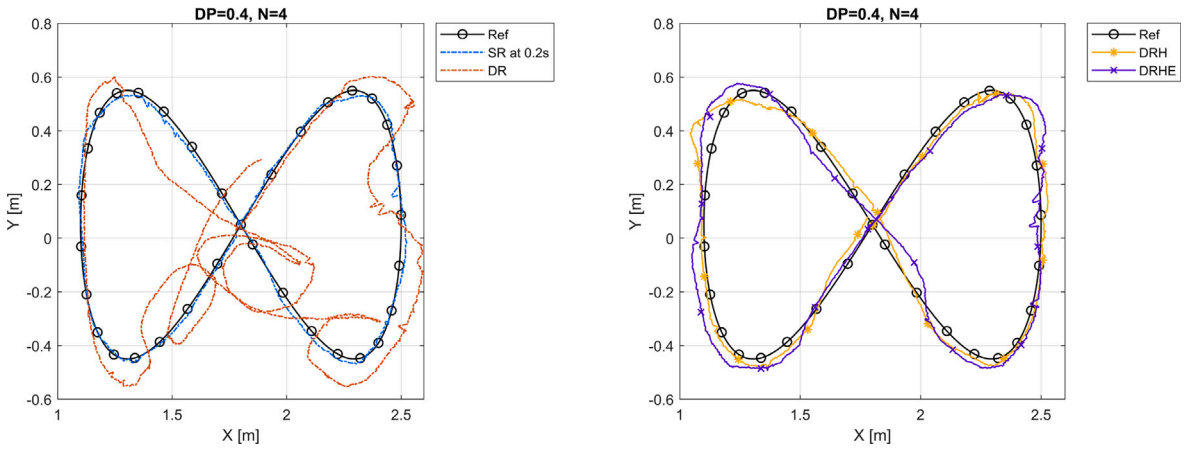

Fig. 12. Path tracking comparison for Lissajous curve in experiments ($DP = 0.4, N = 4$).

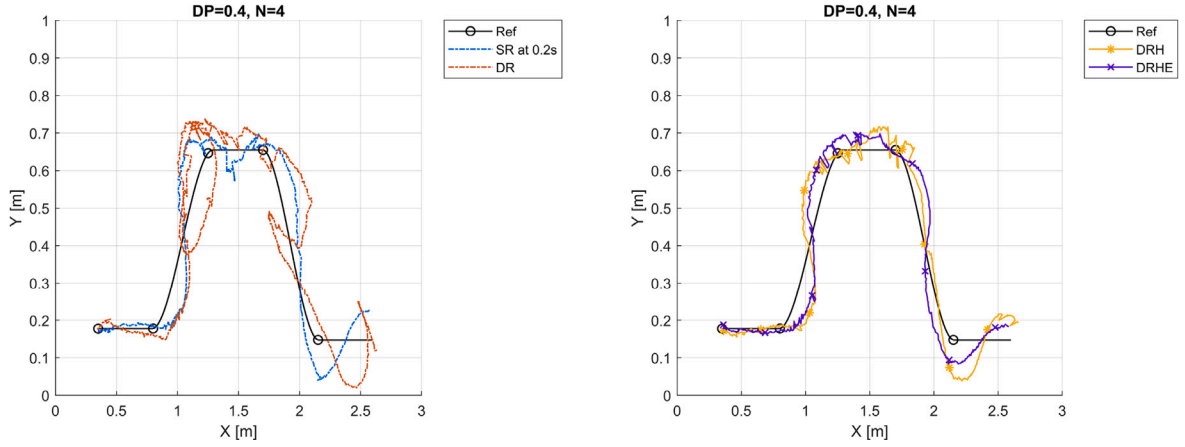

Fig. 13. Path tracking comparison for a double lane change maneuver in experiments ($DP = 0.4, N = 4$).

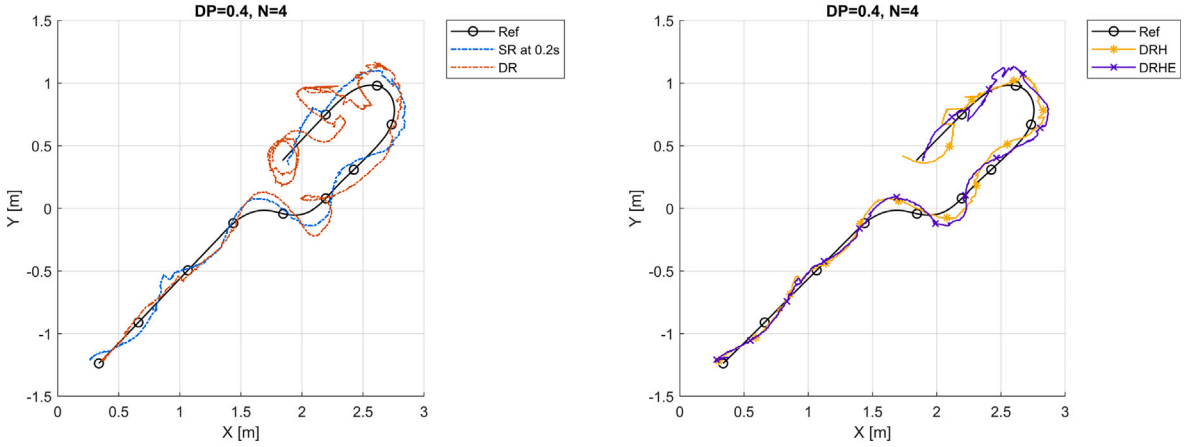

Fig. 14. Path tracking comparison for a 180° turn in experiments ($DP = 0.4, N = 4$).

(20% in simulation). This may be due to the reduced subset of instances used in experimentation, which may benefit the average in this case. As in simulation, the results imply an acceptable performance deterioration for DRHE.

- J_4 is ranging from 0.092 (for $N = 6$ and $DP = 0$) to 0.192 (for $N = 2$ and $DP = 0.4$), which means a significant reduction in resource usage (between 81% and 91%) with respect to the nominal SR approach. This range is very similar to that obtained in simulation (from 87% for $N = 2$ to 91% for $N = 6$). Comparing DRHE with DRH, for $N = 2$ the average reduction arrives approximately at 64%, while for $N = 6$ at 46%. In simulation, the reduction reached is a bit higher for $N = 2$ (76%), but the same for $N = 6$.

As a summary, the experimentation validates the excellent trade-off between control performance and resource usage reduction, which can be attained by the control solution proposed in this work.

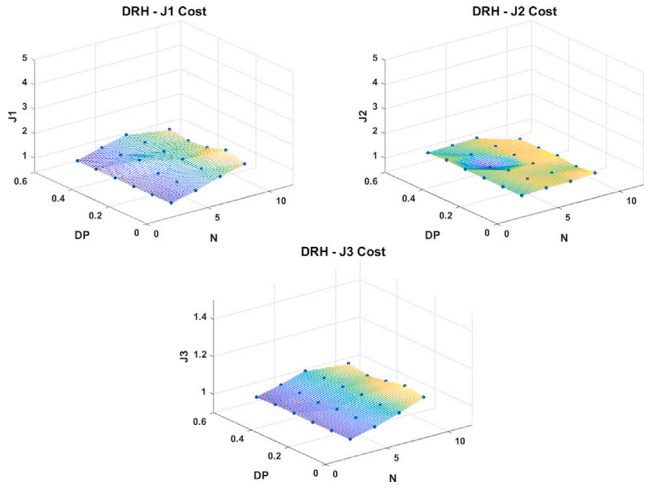

Fig. 15. Experimental results for dual-rate with h-step stage (DRH).

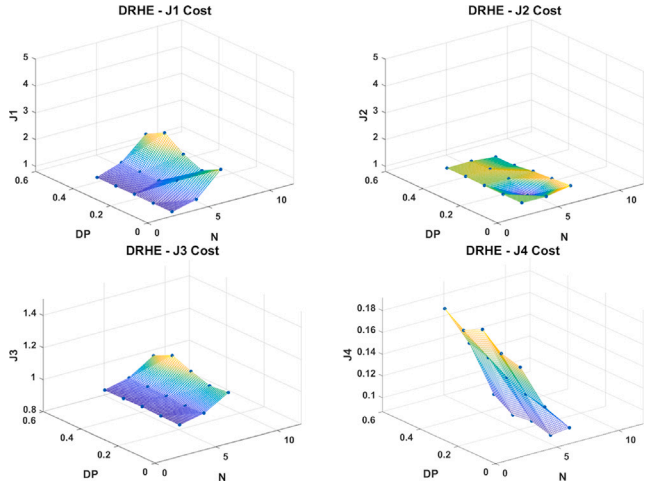

Fig. 16. Experimental results for dual-rate with h-step stage and events (DRHE).

Table 5
Results for J_1 and J_2 in experimentation.

J_1		DRH	DRHE	J_2		DRH	DRHE
DP	N			DP	N		
0	2	1.00	1.05	0	2	1.00	1.04
0.2	2	1.01	1.12	0.2	2	1.02	1.11
0.4	2	1.10	1.23	0.4	2	1.04	1.22
0	6	1.54	1.97	0	6	1.05	1.11
0.2	6	1.55	1.99	0.2	6	1.06	1.17
0.4	6	1.65	2.10	0.4	6	1.19	1.51

Table 6
Results for J_3 and J_4 in experimentation.

J_3		DRH	DRHE	J_4		DRH	DRHE
DP	N			DP	N		
0	2	1.00	1.01	0	2	0.500	0.170
0.2	2	1.01	1.02	0.2	2	0.500	0.188
0.4	2	1.02	1.05	0.4	2	0.500	0.192
0	6	1.07	1.11	0	6	0.167	0.092
0.2	6	1.08	1.13	0.2	6	0.167	0.093
0.4	6	1.09	1.15	0.4	6	0.167	0.101

6. Conclusions

A novel remote control structure based on a systematic integration of estimation, communication, sampling and control techniques is introduced in a wireless networked control framework. The main goal of the proposal is to reach resource efficiency while keeping a satisfactory path-following behavior for a holonomic Mecanum-wheeled robot. Mean-square stability conditions for a non-uniform dual-rate extended Kalman filter are given. A powerful simulation application allows us to reveal the main benefits of the control solution compared to conventional approaches. As a summary, reductions in resource usage of up to 93% are shown in comparison with a nominal time-triggered control approach. As a result, the control design is able to work under low bandwidth conditions, and face a lack of consecutive information for up to 15.6 s, which may be due to a relevant number of consecutive packets dropouts, or long delays. Experimental evaluation validates the results observed in simulation.

As future works, the control solution may be tested using other kind of sensing technology (lidar, GPS, etc.) in order to consider wider paths, even outdoor. With the aim of reaching a real-world implementation, which may involve multiple robots, some crucial aspects such as communication between robots for information exchange, collision avoidance strategies for safe operation, and mechanisms for consensus and coordination to achieve collective goals should be considered. Finally, dynamic event-triggered communication mechanisms may be included in order to explore possible further reductions in resource usage.

CRediT authorship contribution statement

Rafael Carbonell: Validation, Software, Investigation, Data curation. **Ángel Cuenca:** Writing – review & editing, Writing – original draft, Formal analysis, Conceptualization. **Julián Salt:** Supervision, Resources, Methodology. **Ernesto Aranda-Escolástico:** Writing – review & editing, Writing – original draft, Investigation, Formal analysis. **Vicente Casanova:** Validation, Software, Resources.

Declaration of competing interest

The authors declare the following financial interests/personal relationships which may be considered as potential competing interests: Rafael Carbonell reports financial support was provided by Spain Ministry of Science and Innovation. Ernesto Aranda reports financial support was provided by Spain Ministry of Science and Innovation. If there are other authors, they declare that they have no known competing financial interests or personal relationships that could have appeared to influence the work reported in this paper.

Acknowledgment

This work was supported by Grant PRE2019-088467 funded by MCIN/AEI/10.13039/501100011033 and by “ESF Investing in your future”, and by the Spanish State Research Agency under Project PID2020-112658RB-I00/AEI/10.13039/501100011033 and by the UNED under Project 2021V/-TAJOV/001.

Appendix A. Proof of Theorem 1

Proof. The proof is divided into three steps. First, an upper bound for the estimation error covariance matrix $\bar{P}^T_{k+1|k+1}$ is obtained. Then, it is shown that $\mathbb{E}\left[\bar{P}^T_{k+1|k+1}\right] \leq \mathbb{E}\left[\hat{P}^T_{k+1|k}\right]$. Finally, it is proved that the prediction error is exponentially bounded in mean square.

Step 1: First, let us apply Taylor series expansion to the nonlinear system such that the following prediction error covariance matrices can be derived:

$$\hat{P}^T_{k+1|k} = A^T_k \bar{P}^T_{k|k}[A^T_k]^\top + L^T_k Q^T_k [L^T_k]^\top, \tag{A.1}$$

$$\hat{P}^T_{xz,k+1} = \hat{P}^T_{k+1|k}[H^T_{k+1}]^\top, \tag{A.2}$$

$$\hat{P}^T_{zz,k+1} = H^T_{k+1}\hat{P}^T_{k+1|k}[H^T_{k+1}]^\top + M^T_k R^T_{k+1}[M^T_k]^\top, \tag{A.3}$$

where $\bar{P}^T_{k|k}$ is the upper bound to be computed. If an event is triggered ($\gamma_{k+1} = 1$) and there is no loss, either real or artificial due to the dual-rate sampling ($\lambda_{k+1} = 1$), the filter degenerates to a standard Kalman filter, and the single-rate estimation error covariance can be written as follows [45]:

$$\hat{P}^T_{k+1|k+1} = \hat{P}^T_{k+1|k} - \hat{P}^T_{xz,k+1}[\hat{P}^T_{zz,k+1}]^{-1}[\hat{P}^T_{xz,k+1}]^\top \text{ for } \gamma_{k+1} = 1 \tag{A.4}$$

In the case of $\gamma_{k+1} = 0$, (13) can be rewritten as

$$\hat{\xi}^T_{k+1|k+1} = \hat{\xi}^T_{k+1|k} + K^T_{k+1}\left(z^T_{k+1} - \hat{z}^T_{k+1}\right) + K^T_{k+1}\left(\bar{z}^T_{k+1} - z^T_{k+1}\right), \tag{A.5}$$

where $\bar{z}^T_{k+1}$ maintains the value during the fast periods of the last received output $\bar{z}^{NT}_{k+1}$. Consequently, the estimation error is

$$\tilde{\xi}^T_{k+1|k+1} = \tilde{\xi}^T_{k+1|k} - K^T_{k+1}\left(z^T_{k+1} - \hat{z}^T_{k+1}\right) - K^T_{k+1}\left(\bar{z}^T_{k+1} - z^T_{k+1}\right). \tag{A.6}$$

Using the Taylor expansion in (16), (A.6) can be approximated by

$$\tilde{\xi}^T_{k+1|k+1} = \left(I - K^T_{k+1}H^T_{k+1}\right)\tilde{x}^T_{k+1|k} - K^T_{k+1}M^T_{k+1}(n_2)^T_{k+1} - K^T_{k+1}\left(\bar{z}^T_{k+1} - z^T_{k+1}\right). \tag{A.7}$$

Now, $\hat{P}^T_{k+1|k+1}$ for $\gamma_{k+1} = 0$ can be computed as

$$\begin{aligned}
\hat{P}^T_{k+1|k+1} =& \mathbb{E}\left[\tilde{\xi}^T_{k+1|k+1}[\tilde{\xi}^T_{k+1|k+1}]^\top\right] = \left(I - K^T_{k+1}H^T_{k+1}\right)\hat{P}^T_{k+1|k}\left(I - K^T_{k+1}H^T_{k+1}\right)^\top \\
&+ K^T_{k+1}M^T_{k+1}R^T_{k+1}[M^T_{k+1}]^\top[K^T_{k+1}]^\top \\
&+ K^T_{k+1}\mathbb{E}\left[\left(\bar{z}^T_{k+1} - z^T_{k+1}\right)\left(\bar{z}^T_{k+1} - z^T_{k+1}\right)^\top\right][K^T_{k+1}]^\top \\
&- \left(I - K^T_{k+1}H^T_{k+1}\right)\mathbb{E}\left[\tilde{\xi}^T_{k+1|k}\left(\bar{z}^T_{k+1} - z^T_{k+1}\right)^\top\right][K^T_{k+1}]^\top \\
&- K^T_{k+1}\mathbb{E}\left[\left(\bar{z}^T_{k+1} - z^T_{k+1}\right)[\tilde{\xi}^T_{k+1|k}]^\top\right]\left(I - K^T_{k+1}H^T_{k+1}\right)^\top \\
&+ K^T_{k+1}\mathbb{E}\left[\left(\bar{z}^T_{k+1} - z^T_{k+1}\right)[(n_2)^T_{k+1}]^\top\right][K^T_{k+1}]^\top \\
&+ K^T_{k+1}\mathbb{E}\left[(n_2)^T_{k+1}\left(\bar{z}^T_{k+1} - z^T_{k+1}\right)^\top\right][K^T_{k+1}]^\top
\end{aligned} \tag{A.8}$$

Using [46, Lemma 1] and the event-triggering condition in (4), the following inequalities are obtained:

$$\begin{aligned}
&- \left(I - K^T_{k+1}H^T_{k+1}\right)\mathbb{E}\left[\tilde{\xi}^T_{k+1|k}\left(\bar{z}^T_{k+1} - z^T_{k+1}\right)^\top\right][K^T_{k+1}]^\top \\
&- K^T_{k+1}\mathbb{E}\left[\left(\bar{z}^T_{k+1} - z^T_{k+1}\right)[\tilde{\xi}^T_{k+1|k}]^\top\right]\left(I - K^T_{k+1}H^T_{k+1}\right)^\top \\
&\le a_1\left(I - K^T_{k+1}H^T_{k+1}\right)\hat{P}^T_{k+1|k}\left(I - K^T_{k+1}H^T_{k+1}\right)^\top \\
&+ a_1^{-1}K^T_{k+1}\mathbb{E}\left[\left(\bar{z}^T_{k+1} - z^T_{k+1}\right)\left(\bar{z}^T_{k+1} - z^T_{k+1}\right)^\top\right][K^T_{k+1}]^\top \\
&\le a_1\left(I - K^T_{k+1}H^T_{k+1}\right)\hat{P}^T_{k+1|k}\left(I - K^T_{k+1}H^T_{k+1}\right)^\top \\
&+ a_1^{-1}K^T_{k+1}\sigma\hat{P}^T_{zz,k+1}[K^T_{k+1}]^\top + a_1^{-1}K^T_{k+1}\delta[K^T_{k+1}]^\top
\end{aligned}$$

and

$$\begin{aligned}
&K^T_{k+1}\mathbb{E}\left[\left(\bar{z}^T_{k+1} - z^T_{k+1}\right)[(n_2)^T_{k+1}]^\top\right][K^T_{k+1}]^\top \\
&+ K^T_{k+1}\mathbb{E}\left[(n_2)^T_{k+1}\left(\bar{z}^T_{k+1} - z^T_{k+1}\right)^\top\right][K^T_{k+1}]^\top \\
&\le a_2K^T_{k+1}R^T_{k+1}[K^T_{k+1}]^\top + a_2^{-1}K^T_{k+1}\sigma\hat{P}^T_{zz,k+1}[K^T_{k+1}]^\top + a_2^{-1}K^T_{k+1}\delta[K^T_{k+1}]^\top.
\end{aligned}$$

Then, for $\gamma_{k+1} = 0$,

$$\begin{aligned}
\bar{P}^T_{k+1|k+1} =& (1+a_1)\left(I - K^T_{k+1}H^T_{k+1}\right)\hat{P}^T_{k+1|k}\left(I - K^T_{k+1}H^T_{k+1}\right)^\top \\
&+ (1+a_2)K^T_{k+1}R^T_{k+1}[K^T_{k+1}]^\top \\
&+ (1+a_1^{-1}+a_2^{-1})K^T_{k+1}\left(\sigma\hat{P}^T_{zz,k+1} + \delta\right)[K^T_{k+1}]^\top
\end{aligned} \tag{A.9}$$

Finally, combining (A.1), (A.2), (A.3), (A.8) and (A.9), it is got

$$\begin{aligned}
\bar{P}^T_{k+1|k+1} =& \hat{P}^T_{k+1|k} - \gamma_{k+1}\lambda_{k+1}\hat{P}^T_{k+1|k}[H^T_{k+1}]^\top \\
&\times \left(H^T_{k+1}\hat{P}^T_{k+1|k}[H^T_{k+1}]^\top + R^T_{k+1}\right)^{-1}H^T_{k+1}\hat{P}^T_{k+1|k} \\
&+ (1-\gamma_k)\Big[(1+a_1)\left(I - K^T_{k+1}H^T_{k+1}\right)\hat{P}^T_{k+1|k}\left(I - K^T_{k+1}H^T_{k+1}\right)^\top \\
&+ (1+a_2)K^T_{k+1}R^T_{k+1}[K^T_{k+1}]^\top \\
&+ (1+a_1^{-1}+a_2^{-1})K^T_{k+1} \\
&\times \left(\sigma H^T_{k+1}\hat{P}^T_{k+1|k}[H^T_{k+1}]^\top + M^T_{k+1}R^T_{k+1}[M^T_{k+1}]^\top + \delta\right)[K^T_{k+1}]^\top\Big]
\end{aligned} \tag{A.10}$$

Step 2: Now, $\bar{P}^T_{k+1|k+1}$ is statistically analyzed. From (A.1) and (A.10), it is obtained

$$\begin{aligned}
\mathbb{E}\left[\hat{P}^T_{k+1|k}\right] =& \mathbb{E}\Big[A^T_k\hat{P}^T_{k|k-1}[A^T_k]^\top + L^T_kQ^T_k[L^T_k]^\top \\
&- \gamma_k\lambda_kA^T_k\hat{P}^T_{k|k-1}[H^T_k]^\top \\
&\times \left(H^T_k\hat{P}^T_{k|k-1}[H^T_k]^\top + R^T_k\right)^{-1}H^T_k\hat{P}^T_{k|k-1}[A^T_k]^\top \\
&+ (1-\gamma_k)A^T_k\Big((1+a_1)\left(I - K^T_kH^T_k\right)\hat{P}^T_{k|k-1}\left(I - K^T_kH^T_k\right)^\top \\
&+ (1+a_2)K^T_kR^T_k[K^T_k]^\top \\
&+ (1+a_1^{-1}+a_2^{-1})K^T_k\Big(\sigma H^T_k\hat{P}^T_{k|k-1}[H^T_k]^\top \\
&+ M^T_kR^T_k[M^T_k]^\top + \delta\Big)[K^T_k]^\top\Big)[A^T_k]^\top\Big]
\end{aligned} \tag{A.11}$$

Let us now recall $\lambda = \mathbb{E}[\lambda_k]$ and assume that γ is the average sensor communication rate [47]. Then, using [48, Lemma, Appendix A2, p.347] with $A = H^T_k\hat{P}^T_{k|k-1}[H^T_k]^\top$ and $B = R^T_k$ yields

$$\begin{aligned}
\mathbb{E}\left[\hat{P}^T_{k+1|k}\right] <& A^T_k\mathbb{E}\left[\hat{P}^T_{k|k-1}\right][A^T_k]^\top + L^T_kQ^T_k[L^T_k]^\top \\
&- \gamma\lambda\left(A^T_k\mathbb{E}\left[\hat{P}^T_{k|k-1}\right][A^T_k]^\top - A^T_k[H^T_k]^{-1}R^T_k[[H^T_k]^{-1}]^\top[A^T_k]^\top\right) \\
&+ \mathbb{E}\Big[(1-\gamma_k)A^T_k\Big((1+a_1)\left(I - K^T_kH^T_k\right)\hat{P}^T_{k|k-1}\left(I - K^T_kH^T_k\right)^\top \\
&+ (1+a_2)K^T_kR^T_k[K^T_k]^\top \\
&+ (1+a_1^{-1}+a_2^{-1})K^T_k\Big(\sigma H^T_k\hat{P}^T_{k|k-1}[H^T_k]^\top \\
&+ M^T_kR^T_k[M^T_k]^\top + \delta\Big)[K^T_k]^\top\Big)[A^T_k]^\top\Big]
\end{aligned} \tag{A.12}$$

Taking into account the assumptions in (18),

$$\begin{aligned}
\mathbb{E}\left[\hat{P}^T_{k+1|k}\right] <& \left(\bar{a}^2 - \gamma\lambda\bar{a}^2 + (1-\gamma)\bar{a}^2(1+a_1)\left(1+\bar{k}\bar{h}\right)^2\right. \\
&+ \left.(1+a_1^{-1}+a_2^{-1})\bar{k}^2\sigma\bar{h}^2\right)\mathbb{E}\left[\hat{P}^T_{k|k-1}\right] \\
&+ \left(\bar{l}^2\bar{q} - \gamma\lambda\bar{a}^2\underline{\mathrm{h}}^2\bar{r} + (1+a_2)\bar{k}^2\bar{r} + \bar{m}^2\bar{r} + \delta\right)\mathcal{I}_n
\end{aligned} \tag{A.13}$$

Now, assuming $\mathbb{E}[\hat{P}^T_{1|0}] > 0$, it is observed that

$$\begin{aligned}
\mathbb{E}\left[\hat{P}^T_{2|1}\right] <& \left(\bar{a}^2 - \gamma\lambda\bar{a}^2 + (1-\gamma)\bar{a}^2(1+a_1)\left(1+\bar{k}\bar{h}\right)^2\right. \\
&+ \left.(1+a_1^{-1}+a_2^{-1})\bar{k}^2\sigma\bar{h}^2\right)\|\hat{P}^T_{1|0}\| \\
&+ \left(\bar{l}^2\bar{q} - \gamma\lambda\bar{a}^2\underline{\mathrm{h}}^2\bar{r} + (1+a_2)\bar{k}^2\bar{r} + \bar{m}^2\bar{r} + \delta\right)\mathcal{I}_n \\
<& c_1c_2\mathcal{I}_n + c_2\mathcal{I}_n,
\end{aligned} \tag{A.14}$$

where

$$c_1 = \bar{a}^2 - \gamma\lambda\bar{a}^2 + (1-\gamma)\bar{a}^2(1+a_1)\left(1+\bar{k}\bar{h}\right)^2 + (1+a_1^{-1}+a_2^{-1})\bar{k}^2\sigma\bar{h}^2,$$

$$c_2 = \max\left\{ \|\hat{P}^T_{1|0}\|, \bar{l}^2\bar{q} - \gamma\lambda\bar{a}^2\underline{h}^2\bar{r} + (1+a_2)\bar{k}^2\bar{r} + \bar{m}^2\bar{r} + \delta \right\}.$$

By induction, it is concluded that

$$\mathbb{E}\left[\hat{P}^T_{k+1|k}\right] < c_2 \sum_{i=0}^{k} c_1^i \mathcal{I}_n. \tag{A.15}$$

Finally, the filter converges if $c_1 < 1$, i.e. if

$$\lambda > \frac{1 - \bar{a}^2 + (1-\gamma)\bar{a}^2(1+a_1)\left(1+\bar{k}\bar{h}\right)^2 + (1+a_1^{-1}+a_2^{-1})\bar{k}^2\sigma\bar{h}^2}{\gamma\bar{a}^2}.$$

Step 3: Define $V^T_{k+1}(\tilde{\xi}^T_{k+1|k}) = [\tilde{\xi}^T_{k+1|k}]^\top [\hat{P}^T_{k+1|k}]^{-1}\tilde{\xi}^T_{k+1|k}$ with real numbers $\underline{p}$ and $\bar{p}$ such that $\frac{1}{\bar{p}}\left[\tilde{\xi}^T_{k+1|k}\right]^2 \le V^T_{k+1}(\tilde{\xi}^T_{k+1|k}) \le \frac{1}{\underline{p}}\left[\tilde{\xi}^T_{k+1|k}\right]^2$. Then, using (11), (12) and (A.7), the conditional expectation is

$$\begin{aligned}
&\mathbb{E}\left[V^T_{k+1}(\tilde{\xi}^T_{k+1|k})|\tilde{x}^T_{k|k-1}\right] \\
&= \mathbb{E}\Bigg[\Big[A_k^T\Big(\big(I - K_k^T H_k^T\big)\hat{x}^T_{k|k-1} - K_k^T(1-\gamma_k)\big((n_2)_k^T + (\bar{z}^T_{k-1} - z_k^T)\big)\Big) \\
&+ L_k^T(n_1)_k^T\Big]^\top \\
&\times [\hat{P}^T_{k+1|k}]^{-1}\Big[A_k^T\Big(\big(I - K_k^T H_k^T\big)\hat{x}^T_{k|k-1} - K_k^T(1-\gamma_k)\big((n_2)_k^T + (\bar{z}^T_{k-1} - z_k^T)\big)\Big) \\
&+ L_k^T(n_1)_k^T\Big]\Bigg] \\
&= \left[A_k^T\left(I - K_k^T H_k^T\right)\hat{x}^T_{k|k-1} + K_k^T(1-\gamma_k)(\bar{z}^T_{k-1} - z_k^T)\right]^\top [\hat{P}^T_{k+1|k}]^{-1} \\
&\times \left[A_k^T\left(I - K_k^T H_k^T\right)\hat{x}^T_{k|k-1} + K_k^T(1-\gamma_k)(\bar{z}^T_{k-1} - z_k^T)\right] \\
&+ \mathbb{E}\left[[(n_2)_k^T]^\top\left(A_k^T K_k^T(1-\gamma_k)\right)^\top [\hat{P}^T_{k+1|k}]^{-1}\left(A_k^T K_k^T(1-\gamma_k)\right)(n_2)_k^T\right] \\
&+ \mathbb{E}\left[[(n_1)_k^T]^\top [L_k^T]^\top [\hat{P}^T_{k+1|k}]^{-1} L_k^T (n_1)_k^T\right].
\end{aligned} \tag{A.16}$$

From (A.1), it can be written

$$\hat{P}^T_{k+1|k} \ge \left(1 + \frac{\underline{l}^2\underline{q}}{\bar{a}^2\bar{p}}\right) A_k^T \bar{P}^T_{k|k} [A_k^T]^\top. \tag{A.17}$$

Now, using [49, Lemma 6.1],

$$\begin{aligned}
&\left[A_k^T\left(\big(I - K_k^T H_k^T\big)\hat{x}^T_{k|k-1}\right)\right]^\top [\hat{P}^T_{k+1|k}]^{-1}\left[A_k^T\left(\big(I - K_k^T H_k^T\big)\hat{x}^T_{k|k-1}\right)\right] \\
&\le (1-\mu)\, V_k^T(\tilde{x}^T_{k|k-1}).
\end{aligned} \tag{A.18}$$

Applying [46, Lemma 1] and (4) yields

$$\begin{aligned}
&\left[A_k^T\left(I - K_k^T H_k^T\right)\hat{x}^T_{k|k-1} + K_k^T(1-\gamma_k)(\bar{z}^T_{k-1} - z_k^T)\right]^\top [\hat{P}^T_{k+1|k}]^{-1} \\
&\times \left[A_k^T\left(I - K_k^T H_k^T\right)\hat{x}^T_{k|k-1} + K_k^T(1-\gamma_k)(\bar{z}^T_{k-1} - z_k^T)\right] \\
&\le (1-\eta) V_k^T(\tilde{x}^T_{k|k-1}) + a_3^{-1}\bar{k}^2\delta,
\end{aligned} \tag{A.19}$$

which satisfies $0 < \eta \le 1$ for appropriate choice of $a_3 > 0$ and $\sigma \ge 0$. Finally, bounding the noise, it is obtained

$$\mathbb{E}\left[V^T_{k+1}(\tilde{\xi}^T_{k+1|k})|\tilde{x}^T_{k|k-1}\right] \le (1-\eta)V_k^T(\tilde{x}^T_{k|k-1}) + \nu. \tag{A.20}$$

Thus, conditions in [50, Definition 2.1, Lemma 2.1] are fulfilled, and the prediction error is exponentially bounded in mean square as

$$\mathbb{E}\left\{\left(\tilde{\xi}^T_{k+1|k}\right)^2\right\} \le \frac{\bar{p}}{\underline{p}}\mathbb{E}\left\{\left(\tilde{\xi}^T_{1|0}\right)^2\right\}(1-\eta)^k + \nu\bar{p}\sum_{i=1}^{k-1}(1-\eta)^i \quad \square \tag{A.21}$$

References

[1] Wang C, Liu X, Yang X, Hu F, Jiang A, Yang C. Trajectory tracking of an omnidirectional wheeled mobile robot using a model predictive control strategy. Appl Sci 2018;8(2):231.

[2] Adăscăliței F, Doroftei I. Practical applications for mobile robots based on mecanum wheels-a systematic survey. Romanian Rev Precis Mech Opt Mechatron 2011;40:21–9.

[3] Peng C, Li F. A survey on recent advances in event-triggered communication and control. Inform Sci 2018;457:113–25.

[4] Sun J, Yang J, Zeng Z. Predictor-based periodic event-triggered control for nonlinear uncertain systems with input delay. Automatica 2022;136:110055.

[5] González A, Cuenca Á, Salt J, Jacobs J. Robust stability analysis of an energy-efficient control in a networked control system with application to unmanned ground vehicles. Inform Sci 2021;578:64–84.

[6] Cuenca A, Antunes DJ, Castillo A, Garcia P, Khashooei BA, Heemels W. Periodic event-triggered sampling and dual-rate control for a wireless networked control system with applications to UAVs. IEEE Trans Ind Electro 2018;66(4):3157–66.

[7] Aranda-Escolástico E, Colombo L, Guinaldo M. Periodic event-triggered targeted shape control of Lagrangian systems with discrete-time delays. ISA Trans 2021;117:139–49.

[8] Wang J, Liu J, Zhang G, Guo S. Periodic event-triggered sliding mode control for lower limb exoskeleton based on human–robot cooperation. ISA Trans 2022;123:87–97.

[9] Benitez-Garcia SE, Villarreal-Cervantes MG, Guerrero-Castellanos JF, Sánchez-Santana JP. Periodic event-triggered control for the stabilization of robotic manipulators. IEEE Access 2020;8:111553–65.

[10] Aranda-Escolástico E, Rodríguez C, Guinaldo M, Guzmán JL, Dormido S. Asynchronous periodic event-triggered control with dynamical controllers. J Franklin Inst 2018;355(8):3455–69.

[11] Fu A, McCann JA. Dynamic decentralized periodic event-triggered control for wireless cyber–physical systems. IEEE Trans Control Syst Technol 2020;29(4):1783–90.

[12] Fan B, Peng J, Yang Q, Liu W. Distributed periodic event-triggered algorithm for current sharing and voltage regulation in DC microgrids. IEEE Trans Smart Grid 2019;11(1):577–89.

[13] Cuenca Á, Zheng M, Tomizuka M, Sánchez S. Non-uniform multi-rate estimator based periodic event-triggered control for resource saving. Inform Sci 2018;459:86–102.

[14] Knapp ED. Industrial Network Security: Securing critical infrastructure networks for smart grid, SCADA, and other Industrial Control Systems. Elsevier; 2024.

[15] Huang J, Zhao M, Zhou Y, Xing C-C. In-vehicle networking: Protocols, challenges, and solutions. IEEE Netw 2018;33(1):92–8.

[16] Li Z, Xia Y, Su C-Y. Intelligent networked teleoperation control. Springer; 2015.

[17] Welch G, Bishop G. An introduction to the Kalman filter. 2006;378.

[18] Coulter RC. Implementation of the pure pursuit path tracking algorithm. Tech. rep., Carnegie-Mellon UNIV Pittsburgh PA Robotics INST; 1992.

[19] Samsuri SB, Zamzuri H, Rahman MAA, Mazlan SA, Rahman A. Computational cost analysis of extended kalman filter in simultaneous localization and mapping (ekf-slam) problem for autonomous vehicle. ARPN J Eng Appl Sci 2015;10(17):153–8.

[20] Sun Y, Xu J, Zhang H. Feedback Nash equilibrium with packet dropouts in networked control systems. IEEE Trans Circuits Syst II: Express Briefs 2023;70(3):1024–8.

[21] Rouamel M, Bourahala F, Guelton K. Relaxed stability analysis and sampled-data controller design for networked control systems with network-induced delays. Trans Inst Meas Control 2022;44(16):3191–205.

[22] Liu D, Wang Z, Liu Y, Alsaadi FE. Extended Kalman filtering subject to random transmission delays: Dealing with packet disorders. Inf Fusion 2020;60:80–6.

[23] Zhan X-S, Zhang W-K, Wu J, Yan H-C. Performance analysis of NCSs under channel noise and bandwidth constraints. IEEE Access 2020;8:20279–88.

[24] Aranda-Escolástico E, Guinaldo M, Miśkowicz M, Dormido S. Event-based control in industry practice: Paving the way toward resource-efficient industrial internet of things. IEEE Ind Electro Magazine 2023;2–11.

[25] Jia X-C. Resource-efficient and secure distributed state estimation over wireless sensor networks: A survey. Int J Syst Sci 2021;52(16):3368–89.

[26] Shibata K, Jimbo T, Matsubara T. Deep reinforcement learning of event-triggered communication and consensus-based control for distributed cooperative transport. Robot Auton Syst 2023;159:104307.

[27] Lozoya C, Favela-Contreras A, Aguilar-Gonzalez A, Félix-Herrán LC, Orona L. Energy-efficient wireless communication strategy for precision agriculture irrigation control. Sensors 2021;21(16):5541.

[28] Abdelrahim M, Almakhles D. Output feedback stabilization of doubly fed induction generator wind turbines under event-triggered implementations. J Sens Actuator Netw 2023;12(5):64.

[29] Li L, Cao Y, Zhao L. Output-based event-triggered tracking control for networked pneumatic muscle actuators system with packet disorders. Nonlinear Dynam 2023;111(7):6363–78.

[30] Hesar HD, Mohebbi M. A multi rate marginalized particle extended Kalman filter for P and T wave segmentation in ECG signals. IEEE J Biomedical and Health Inf 2018;23(1):112–22.

[31] Zhao Y-B, Liu G-P, Kang Y, Yu L. Packet-based control design for networked control systems. In: Packet-based control for networked control systems. Springer; 2018, p. 15–32.

[32] Gopalakrishnan A, Kaisare NS, Narasimhan S. Incorporating delayed and infrequent measurements in extended Kalman filter based nonlinear state estimation. J Process Control 2011;21(1):119–29.
[33] Wang J, Alipouri Y, Huang B. Multirate sensor fusion in the presence of irregular measurements and time-varying time delays using synchronized, neural, extended Kalman filters. IEEE Trans Instrum and Measur 2021;71:1–9.
[34] Pizá R, Carbonell R, Casanova V, Cuenca Á, Salt Llobregat JJ. Nonuniform dual-rate extended Kalman-filter-based sensor fusion for path-following control of a holonomic mobile robot with four mecanum wheels. Appl Sci 2022;12(7):3560.
[35] Alite G, Cuenca Á, Salt J, Tomizuka M. Resource-efficient path-following control for a self-driving car in a networked control system. IEEE Access 2023;11:108011–23.
[36] Dosoftei C, Horga V, Doroftei I, Popovici T, Custura Ş. Simplified mecanum wheel modelling using a reduced omni wheel model for dynamic simulation of an omnidirectional mobile robot. In: Int. conf. and expos. on electrical and power eng.. IEEE; 2020, p. 721–6.
[37] Bayar G, Ozturk S. Investigation of the effects of contact forces acting on rollers of a mecanum wheeled robot. Mechatronics 2020;72:102467.
[38] Siegwart R, Nourbakhsh I, Scaramuzza D. Introduction to Autonomous Mobile Robots, 2nd ed. MIT Press; 2011.
[39] Rajamani R. Vehicle dynamics and control. Springer Science & Business Media; 2011.
[40] Cotera P, Velazquez M, Cruz D, Medina L, Bandala M. Indoor robot positioning using an enhanced trilateration algorithm. Int J Advanced Robotic Syst 2016;13(3):110.
[41] Borgers DP, Heemels WMH. Event-separation properties of event-triggered control systems. IEEE Trans Autom Control 2014;59(10):2644–56.
[42] Xing L, Wen C, Liu Z, Su H, Cai J. Event-triggered adaptive control for a class of uncertain nonlinear systems. IEEE Trans Autom Control 2017;62(4):2071–6.
[43] Hervé SA, Aurelien YT, Leandre NN, Som IJH. Improved networked iterative learning fault-tolerant control algorithm for systems with time-delays, random packet losses, limited communication and actuator failure. Int J Control, Autom and Syst 2022;1–9.
[44] Tipsuwan Y, Chow M. Gain scheduler middleware: a methodology to enable existing controllers for networked control and teleoperation-part I: networked control. IEEE Trans Ind Electro 2004;51(6):1218–27.
[45] Julier SJ, Uhlmann JK. Unscented filtering and nonlinear estimation. Proc IEEE 2004;92(3):401–22.
[46] Li L, Yu D, Xia Y, Yang H. Event-triggered UKF for nonlinear dynamic systems with packet dropout. Int J Robust and Nonlinear Control 2017;27(18):4208–26.
[47] Han D, Mo Y, Wu J, Weerakkody S, Sinopoli B, Shi L. Stochastic event-triggered sensor schedule for remote state estimation. IEEE Trans Autom Control 2015;60(10):2661–75.
[48] Lewis FL. Optimal estimation. New York, USA: Wiley; 1986.
[49] Kluge S, Reif K, Brokate M. Stochastic stability of the extended Kalman filter with intermittent observations. IEEE Trans Autom Control 2010;55(2):514–8.
[50] Reif K, Gunther S, Yaz E, Unbehauen R. Stochastic stability of the discrete-time extended Kalman filter. IEEE Trans Autom Control 1999;44(4):714–28.